View metadata, citation and similar papers at core.ac.uk

brought to you by CORE

provided by IntechOpen

We are IntechOpen, the world's leading publisher of Open Access books Built by scientists, for scientists

4,800
Open access books available

122,000
International authors and editors

135M
Downloads

Our authors are among the

154
Countries delivered to

TOP 1%
most cited scientists

12.2%
Contributors from top 500 universities

CLARIVATE ANALYTICS BOOK CITATION INDEX INDEXED

WEB OF SCIENCE™

Selection of our books indexed in the Book Citation Index in Web of Science™ Core Collection (BKCI)

Interested in publishing with us?
Contact book.department@intechopen.com

Numbers displayed above are based on latest data collected.
For more information visit www.intechopen.com

Chapter 1

Hybrid Laser-Arc Welding

J. Zhou and H.L. Tsai

Additional information is available at the end of the chapter

http://dx.doi.org/10.5772/50113

1. Introduction

Hybrid laser-arc welding has received increasing interest in both academia and industry in last decade[1,2]. As shown in Fig. 1, hybrid laser-arc welding is formed by combining laser beam welding and arc welding. Due to the synergic action of laser beam and welding arc, hybrid welding offers many advantages over laser welding and arc welding alone[3-6], such as high welding speed, deep penetration[7], improved weld quality with reduced susceptibility to pores and cracks[8-16], excellent gap bridging ability[17-22], as well as good process stability and efficiency, as shown in Fig. 2.

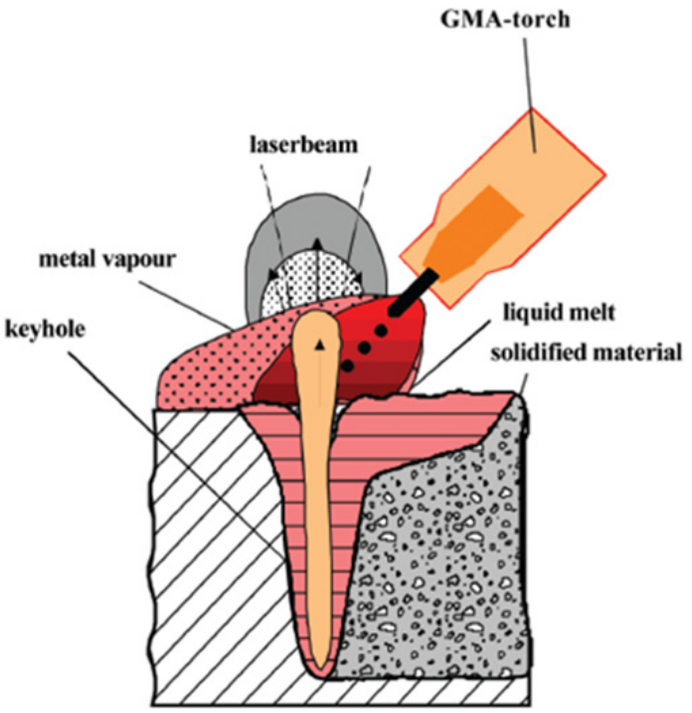

Figure 1. Schematic sketch of a hybrid laser-arc welding process.

INTECH
open science | open minds

© 2012 Zhou and Tsai, licensee InTech. This is an open access chapter distributed under the terms of the Creative Commons Attribution License (http://creativecommons.org/licenses/by/3.0), which permits unrestricted use, distribution, and reproduction in any medium, provided the original work is properly cited.

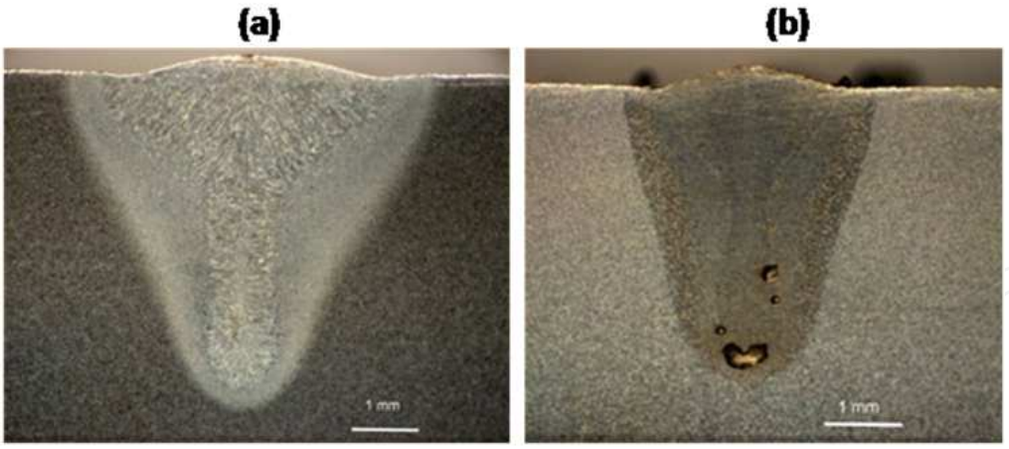

Figure 2. Comparison between (a) a laser weld and (b) a hybrid laser-arc weld in 250 grade mild steel.

Development of the hybrid laser-arc welding technique can be divided into three stages[1]. The concept of hybrid laser welding was first proposed by Steen *et al*.[3, 23, 24] in the late seventies. In their studies, a CO_2 laser was combined with a tungsten inert gas (TIG) arc for welding and cutting applications. Their tests showed clear benefits of combining an arc and a laser beam in the welding process, such as a stabilized arc behavior under the influence of laser radiation; a dramatic increase in the speed of welding of thin metal sheets; and an increase in penetration depth compared with laser welding. Japanese researchers continued Steen's effort and developed various methods and corresponding devices for laser-arc welding, cutting, and surface treatment. However, these efforts did not advance this joining technique into engineering applications particularly because laser welding itself was not yet an economic and viable joining technique at that time[25]. In the second stage of the development of the hybrid laser-arc welding technique, the observed influence of the arc column behavior by laser radiation was used to improve the efficiency of arc welding processes, which leads to the laser-enhanced arc welding technology[1]. A characteristic feature of this technology was that only a low-intensity laser beam was needed, i.e., the required laser power was small compared to the arc power. For TIG welding, Cui and Decker[26-28] demonstrated that a low-energy CO_2 laser beam with a power of merely 100 W could facilitate arc ignition; enhance arc stability; improve weld quality; and increase welding speed due to a reduced arc size and higher arc amperages. However, despite such reported improvements of the arc welding process through laser support, there were neither subsequent extensive investigations of this subject nor known industrial applications of the laser-enhanced arc welding technology. The third stage of hybrid welding technology started in the early 1990s with the development of combined welding processes using a high-power laser beam as the primary and an additional electric arc as the secondary heating source[29-37]. At that time, although the continuous wave CO_2 laser welding process was already well established in industry, it had some known disadvantages, e.g., high requirements of edge preparation and clamping; fast solidification leading to material-dependent pores and cracks; as well as the high investment and operating costs for the laser equipment. Additionally, some welding applications of highly practical interest could not be

solved satisfactorily by the laser welding process alone, e.g., joining of tailored blanks in the automotive engineering; welding of heavy plates in shipbuilding industry; as well as high speed welding of crack-susceptible materials. In searching for suitable solutions, the hybrid laser welding was developed into a viable joining technique with significant industrial acceptance during the last decade.

According to the combination of various heating sources used, hybrid welding can be generally categorized as: (1) laser-gas tungsten arc (GTA) welding; (2) laser-gas metal arc (GMA) welding; and (3) laser-plasma welding[25]. Since laser welding offers deep penetration, primary heating sources commonly used in hybrid welding are CO_2, Nd:YAG, and fiber lasers. The first two types of lasers are well established in practice and used for various hybrid welding process developments. While the fiber laser is still in development for industrial applications, it seems to be a future primary heating source for hybrid welding due to its high beam quality. The secondary heating sources used in hybrid welding are mainly electric arcs. Dedicated processes can be divided into GMA welding with consumable electrodes and GTA welding with non-consumable tungsten electrodes. In GMA welding, the arc is burning between a mechanically supplied wire electrode and the workpiece. The shielding gas used in GMA welding was found to have significant effects on arc shape and metal transfer[38,39]. Hence, GMA welding can be subdivided into metal inert-gas (MIG) and metal active-gas (MAG) welding according to the type of shielding gas used. In GTA welding, a chemically inert gas, such as argon or helium, is often used. A special form of this is the plasma arc welding (PAW), which produces a squeezed arc due to a special torch design and results in a more concentrated arc spot.

In hybrid welding, laser and arc are arranged preferably in a way that they can compensate and benefit from each other during the welding process, which implies the creation of a common interaction zone with changed characteristics in comparison to the laser welding and the arc welding alone. In contrast to this is the arrangement in which laser and arc are serving as two separate heating sources during the welding process. Several configurations have been proposed. In a parallel arrangement, there is a distance in either the vertical or horizontal direction along the path between both heating sources. In a serial arrangement, the primary and secondary heating sources are moved along the same welding path with a certain working distance, and the secondary heating source can either lead or follow the primary heating source[1]. The first one enables a preheating of the region to be welded. It can increase the efficiency of the laser welding process because materials to be welded are locally preheated and energy losses through heat conduction are reduced. In comparison, the second one often acts like a short-time post-heat treatment of the weld that can change the weld microstructure favorably. There exists a key difference between parallel and serial process arrangement. In a serial arrangement, additional energy is dissipated within the weld seam region, whereas in the parallel arrangement, the heat flow is reduced only across the weld seam. The option to move the working area temporally enables flexibility in influencing the cooling rates in order to avoid defects.

In the hybrid laser-arc welding process, the workpiece is first heated up and melted due to the laser irradiation. The plasma arc between the consumable electrode and the workpiece continues to heat up and melt the base metal and the droplets generated at the electrode tip periodically detach and impinge onto the workpiece. Then a cavity with large depth-to-width ratio called keyhole was formed in the weld pool under the dynamical interaction of laser irradiation, plasma arc and filler droplets. An externally supplied shielding gas provides the protection of molten metal from exposing to the atmosphere. The successive weld pools create a weld bead and become a part of a welded joint when solidified. The numbers of process parameters are greatly increased in the hybrid welding, mainly including laser beam parameters, electric power parameters, laser-arc interval, electrode diameter, wire feed speed, welding speed and shielding gas. Bagger and Olsen[66] reviewed the fundamental phenomena occurring in laser-arc hybrid welding and the principles for choosing the process parameters. Ribic *et al.*[67] reviewed the recent advances in hybrid welding with emphases on the physical interactions between laser and arc, and the effects of the combined laser-arc heat source on the welding process.

Current understanding of hybrid laser-arc welding is primarily based on experimental observations. Hybrid laser-arc welding is restricted to specific applications, predominantly the joining of thick section plain carbon steels. In order to expand the applications of this joining technique and optimize the processes for its current applications, fundamental understanding of the transport phenomena and the role of each parameter becomes critical. Numerical investigations were often carried out for this purpose. Ribic *et al.*[67] developed a three-dimensional heat transfer and fluid flow model for laser-GTA hybrid welding to understand the temperature field, cooling rates and mixing in the weld pool. Kong and Kovacevic[68] developed a three-dimensional model to simulate the temperature field and thermally induced stress field in the workpiece during the hybrid laser-GTA process. Mathematical models have also been developed to simulate the weld pool formation and flow patterns in hybrid laser-GMA welding by incorporating free surfaces based on the VOF method. Generally, the typical phenomena in GMA welding such as droplets impingement into the weld pool, electromagnetic force in the weld pool and the typical phenomena in laser beaming welding such as keyhole dynamics, inverse Bremsstrahlung absorption and Fresnel absorption were considered in these models. Surface tension, buoyancy, droplet impact force and recoil pressure were considered to calculate the melt flow patterns. In the following, fundamental physics, especially transport phenomena involved in hybrid laser-arc welding will be elaborated.

2. Fundamentals of hybrid laser-arc welding

Since hybrid laser-arc welding involves laser welding, arc welding and their interactions as well, complicated physical processes like metal melting and solidification; melt flow; keyhole plasma formation; arc plasma formation and convection are typically involved, which results in very complex transport phenomena in this welding process[40]. As known,

transport phenomena in welding, such as heat transfer; melt flow; and plasma flow, can strongly affect both metallurgical structures and mechanical properties of the weld[41-45]. In the following, transport phenomena in hybrid welding will be discussed and particular attentions are given to 1) arc plasma formation and its effect on metal transfer and weld pool dynamics; 2) laser-induced plasma formation and laser-plasma interaction; 3) recoil pressure and other possible mechanisms contributing to keyhole formation and dynamics; 4) the interplay among various process parameters; and 5) plasma - filler metal - weld pool interactions.

Due to the different natures of heat and mass transfer mechanisms in metal and plasma, different models are developed to study the fundamental physics in hybrid laser-arc welding. One is for the metal region containing base metal, electrode, droplets, and arc plasma. The other is for the keyhole region containing laser-induced plasma. There is a free surface (liquid/vapor interface) separating these two regions. For the metal region, continuum formation is used to calculate the energy and momentum transport[40]. For the keyhole plasma region, laser-plasma interaction and the laser energy absorption mechanism will be discussed. These two regions are coupled together and the VOF technique is used to track the interface between these two regions[40].

2.1. Transport phenomena in metal (electrode, droplets, and workpiece) and arc plasma

Differential equations governing the conservation of mass, momentum and energy based on continuum formulation are given below[46]:

Conservation of mass

$$\frac{\partial}{\partial t}(\rho)+\nabla\cdot(\rho \boldsymbol{V})=0 \tag{1}$$

where t is the time, ρ is the density, and V is the velocity vector.

Conservation of momentum

$$\begin{aligned}\frac{\partial}{\partial t}(\rho u)+\nabla\cdot(\rho \boldsymbol{V} u)=\nabla\cdot\left(\mu_l\frac{\rho}{\rho_l}\nabla u\right)-\frac{\partial p}{\partial x}-\frac{u_l}{K}\frac{\rho}{\rho_l}(u-u_s)-\frac{C\rho^2}{K^{0.5}\rho_l}|u-u_s|(u-u_s)\\ -\nabla\cdot(\rho f_s f_l \boldsymbol{V_r} u_r)+\nabla\cdot\left(\mu_s u\nabla\left(\frac{\rho}{\rho_l}\right)\right)+\boldsymbol{J}\times\boldsymbol{B}\big|_x\end{aligned} \tag{2}$$

$$\begin{aligned}\frac{\partial}{\partial t}(\rho v)+\nabla\cdot(\rho \boldsymbol{V} v)=\nabla\cdot\left(\mu_l\frac{\rho}{\rho_l}\nabla v\right)-\frac{\partial p}{\partial y}-\frac{u_l}{K}\frac{\rho}{\rho_l}(v-v_s)-\frac{C\rho^2}{K^{0.5}\rho_l}|v-v_s|(v-v_s)\\ -\nabla\cdot(\rho f_s f_l \boldsymbol{V_r} v_r)+\nabla\cdot\left(\mu_s v\nabla\left(\frac{\rho}{\rho_l}\right)\right)+\boldsymbol{J}\times\boldsymbol{B}\big|_y\end{aligned} \tag{3}$$

$$\frac{\partial}{\partial t}(\rho w)+\nabla\cdot(\rho \boldsymbol{V} w)=\rho g+\nabla\cdot\left(\mu_l\frac{\rho}{\rho_l}\nabla w\right)-\frac{\partial p}{\partial z}-\frac{u_l}{K}\frac{\rho}{\rho_l}(w-w_s)-\frac{C\rho^2}{K^{0.5}\rho_l}\left|w-w_s\right|(w-w_s)$$
$$-\nabla\cdot(\rho f_s f_l \boldsymbol{V_r} w_r)+\nabla\cdot\left(\mu_s w\nabla\left(\frac{\rho}{\rho_l}\right)\right)+\rho g\beta_T(T-T_0)+F_{drag}+\mathbf{J}\times\mathbf{B}\Big|_z \quad (4)$$

where u, v and w are the velocities in the x-, y- and z-directions, respectively, and $\mathbf{V_r}$ is the relative velocity vector between the liquid phase and the solid phase. $\mathbf{J}$ is the current field vector and $\mathbf{B}$ is the magnetic field vector. The subscripts s and l refer to the solid and liquid phases, respectively; Subscript 0 represents the reference conditions; p is the pressure; μ is the viscosity; f is the mass fraction; K, the permeability, is a measure of the ease with which fluid passes through the porous mushy zone; C is the inertial coefficient; β_T is the thermal expansion coefficient; g is the gravitational acceleration; and T is the temperature.

Conservation of energy

$$\frac{\partial}{\partial t}(\rho h)+\nabla\cdot(\rho \mathbf{V} h)=\nabla\cdot\left(\frac{k}{c_p}\nabla h\right)-\nabla\cdot\left(\frac{k}{c_p}\nabla(h_s-h)\right)-$$
$$-\nabla\cdot\left(\rho(\mathbf{V}-\mathbf{V_s})(h_l-h)\right)+\frac{|\mathbf{J}|}{\sigma_e}-S_R+\frac{5k_b}{2e}\mathbf{J}\cdot\frac{\nabla h}{c_p} \quad (5)$$

where h is the enthalpy, k is the thermal conductivity, and c_p is the specific heat. The first two terms on the right-hand side of Eq. (5) represent the net Fourier diffusion flux. The third term represents the energy flux associated with the relative phase motion. σ_e is the electrical conductivity; S_R is the radiation heat loss; k_b is the Stefan-Boltzmann constant; and e is the electronic charge.

The third and fourth terms on the right-hand side of Eqs. (2)-(4) represent the first and second order drag forces of the flow in the mushy zone. The fifth term represents an interaction between the solid and the liquid phases due to the relative velocity. The second term on the right hand side of Eq. (5) represents the net Fourier diffusion flux. The third term represents the energy flux associated with the relative phase motion. All these aforementioned terms in this paragraph are zero except in the mushy zone. In addition, the solid phase is assumed to be stationary (V_S= 0).

Conservation of species

$$\frac{\partial}{\partial t}(\rho f^\alpha)+\nabla\cdot(\rho \mathbf{V} f^\alpha)=\nabla\cdot\left(\rho D\nabla f^\alpha\right)-\nabla\cdot\left(\rho D\nabla\left(f_l^\alpha-f^\alpha\right)\right)-\nabla\cdot\left(\rho(\mathbf{V}-\mathbf{V_s})\left(f_l^\alpha-f^\alpha\right)\right) \quad (6)$$

where D is a mass diffusivity and f^α is a mass fraction of constitute. Subscript, l and s, represents liquid and solid phase respectively.

2.2. Transport phenomena in laser induced plasma

The vapor inside the keyhole is modeled as a compressible, inviscid ideal gas. No vapor flow is assumed in the keyhole and the energy equation is given in the following form[47]:

$$\frac{\partial}{\partial t}(\rho_v h_v) = \nabla \cdot \left(\frac{k_v}{c_v} \nabla h_v \right) + \nabla \cdot (-\mathrm{q_r}) + k_{pl} \cdot I_{laser} \cdot (1-\alpha_{iB,1}) + \\ + \sum_{mr=1}^{n} k_{pl} I_{laser} \cdot (1-\alpha_{iB,1}) \cdot (1-\alpha_{Fr}) \cdot (1-\alpha_{iB,mr}) \tag{7}$$

where h_v and ρ_v represent the enthalpy and density of the plasma; k_v and c_v represent the thermal conductivity and specific heat of the plasma. The first term on the right-hand side of Eq. (7) represents the heat conduction term. The second term represents the radiation heat term and q_r stands for the radiation heat flux vector. The fourth term represents energy input from the original laser beam. The last term represents the energy input from multiple reflections of the laser beam inside the keyhole.

2.3. Electrical potential and magnetic field

Arc plasma from GMA welding will not only provide heat to the base metal, but will also exert magnetic force on the weld pool. The electromagnetic force can be calculated as follows[48]:

Conservation of current

$$\nabla \cdot (\sigma_e \nabla \phi) = 0 \tag{8}$$

$$\boldsymbol{J} = -\sigma_e \nabla \phi \tag{9}$$

where ϕ is the electrical potential. According to Ohm's law, the self-induced magnetic field B_θ is calculated by the following Ampere's law:

$$B_\theta = \frac{\mu_0}{r} \int_0^r j_z r dr \tag{10}$$

where μ_0 = 4π x 10^{-7} H m^{-1} is the magnetic permeability of free space. Finally, three components of the electromagnetic force in Eqs. (2)-(4) are calculated via

$$\mathbf{J} \times \mathbf{B}\big|_x = -B_\theta j_z \frac{x - x_a}{r} \tag{11}$$

$$\mathbf{J} \times \mathbf{B}\big|_y = -B_\theta j_z \frac{y}{r} \tag{12}$$

$$\mathbf{J} \times \mathbf{B}\big|_z = -B_\theta j_r \tag{13}$$

2.4. Arc plasma and its interaction with metal zone (electrode, droplets, and weld pool)

In welding, shielding gas is ionized and forms a plasma arc between the electrode and workpiece. In the arc region, the plasma is assumed to be in local thermodynamic equilibrium (LTE)[49], implying the electron and the heavy particle temperatures are equal. On this basis, the plasma properties, including enthalpy, specific heat, density, viscosity, thermal conductivity and electrical conductivity, are determined from an equilibrium composition calculation[49]. It is noted that the metal vaporized from the metal surface may influence plasma material properties, but this effect is omitted in the present study. It is also assumed that the plasma is optically thin, thus the radiation may be modeled in an approximate manner by defining a radiation heat loss per unit volume[49]. The transport phenomena in the arc plasma and the metal are calculated separately in the corresponding arc domain and metal domain, and the two domains are coupled through interfacial boundary conditions in each time step.

Heat transfer

At the plasma-electrode interface, there exists an anode sheath region[49]. In this region, the mixture of plasma and metal vapor departs from LTE, thus it no longer complies with the model presented above. Since the sheath region is very thin, it is treated as a special interface to take into account the thermal effects on the electrode. The energy balance equation at the surface of the anode is modified to include an additional source term, S_a,[50,51] for the metal region.

$$S_a = \frac{k_{eff}(T_{arc}-T_a)}{\delta} + J_a\phi_w - q_{rad} - q_{evap} \tag{14}$$

The first term on the right-hand side of Eq. (14) is the contribution due to heat conduction from the plasma to the anode. The symbol k_{eff} represents the thermal conductivity taken as the harmonic mean of the thermal conductivities of the arc plasma and the anode material. δ is the length of the anode sheath region. T_{arc} is the arc temperature and T_a is the temperature of the anode. The second term represents the electron heating associated with the work function of the anode material. J_a is the current density at the anode and ϕ_w is the work function of the anode material. The third term q_{rad} is the black body radiation loss from the anode surface. The final term q_{evap} is the heat loss due to the evaporation of electrode materials.

Similar to the anode region, there exists a cathode sheath region between the plasma and the cathode. However, the physics of the cathode sheath and the energy balance at the nonthermionic cathode for GMA welding are not well understood[50-56]. The thermal effect due to the cathode sheath has been omitted in many models and reasonable results were obtained[50-54]. Thus, the energy balance equation at the cathode surface will only have the conduction, radiation, and evaporation terms.

$$S_a = \frac{k_{eff}(T_{arc}-T_c)}{\delta} - q_{rad} - q_{evap} \tag{15}$$

where k_{eff} is the effective thermal conductivity at the arc-cathode surface taken as the harmonic mean of the thermal conductivities of the arc plasma and the cathode material. δ is the length of the cathode sheath. T_c is the cathode surface temperature.

Force balance

The molten part of the metal is subjected to body forces, such as gravity and electromagnetic force. It is also subjected to surface forces, such as surface tension due to surface curvature, Marangoni shear stress due to temperature difference, and arc plasma shear stress and arc pressure at the interface of arc plasma and metal. For cells containing a free surface, surface tension pressure normal to the free surface can be expressed as[57]

$$p_s = \gamma\kappa \tag{16}$$

where γ is the surface tension coefficient and κ is the free surface curvature.

The temperature-dependent Marangoni shear stress at the free surface in a direction tangential to the local free surface is given by[58]

$$\boldsymbol{\tau}_{Ms} = \frac{\partial\gamma}{\partial T}\frac{\partial T}{\partial \boldsymbol{s}} \tag{17}$$

where s is a vector tangential to the local free surface.

The arc plasma shear stress is calculated at the free surface from the velocities of arc plasma cells immediately adjacent the metal cells

$$\boldsymbol{\tau}_{ps} = \mu\frac{\partial \boldsymbol{V}}{\partial T} \tag{18}$$

where μ is the viscosity of arc plasma.

The arc pressure at the metal surface is obtained from the computational result in the arc region. The surface forces are included by adding source terms to the momentum equations according to the CSF (continuum surface force) model[57]. Using F of the VOF function as the characteristic function, surface tension pressure, Marangoni shear stress, arc plasma shear stress, and arc pressure are all transformed to the localized body forces and added to the momentum transport equations as source terms for the boundary cells. Based on these assumptions, Hu *et al.* has successfully simulated the arc and droplet formation and effects of current density and the type of shielding gas on arc formation in a GMA welding process, as shown in Fig. 3.

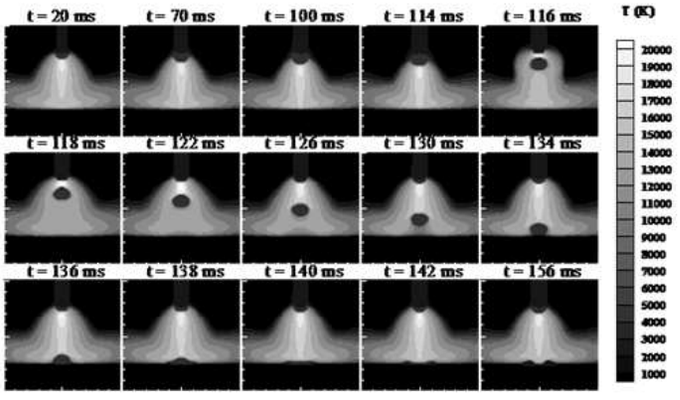

Figure 3. Arc formation in a GMA welding process.

2.5. Laser-induced recoil pressure and keyhole dynamics

In the laser welding process, the laser beam is directed to the metal surface, which first melts the material and produces a small molten pool in the workpiece. The liquid metal is then heated to high temperatures resulting in large evaporation rates. The rapid evaporation creates a large recoil pressure on the surface of the molten layer depressing it downwards. Thus, a cavity with large depth-to-width ration called keyhole is formed. Many investigators believe that the balance between the recoil pressure and surface tension force determines the shape of the keyhole. So, understanding the formation and behavior of the recoil pressure becomes very important for studying the laser welding process. The recoil pressure results from the rapid evaporation of the liquid metal surface. When the liquid metal on the surface is heated to its boiling point, evaporation begins to occur. There is a very thin layer called Knudsen layer adjacent to the liquid surface where the vapor escaping from the liquid surface is in a state of thermodynamic non-equilibrium, i.e., the vapor molecules do not have a Maxwellian velocity distribution. This occurs when the equilibrium vapor pressure (i.e., the saturation pressure) corresponding to the surface temperature is large compared to the ambient partial pressure of the vapor. Under these conditions the vapor adjacent to the surface is dominated by recently evaporated material that has not yet experienced the molecular collisions necessary to establish a Maxiwellian velocity distribution. The Knudsen layer is estimated to be a few molecular mean free paths thick in order to allow for the molecular collisions to occur that bring the molecules into a state of translational equilibrium at the outer edge of the Knudsen layer. The flow field around the Knudsen layer is shown in Fig. 4.

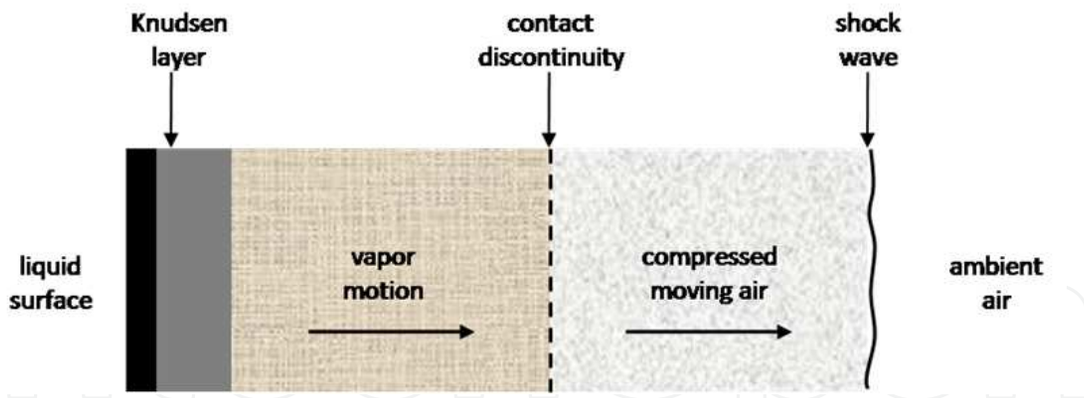

Figure 4. A schematic of the gas dynamic of vapor and air away from a liquid surface at elevated temperature.

Anisimov[59] and Knight[60] did the early investigations on the Knudsen layer. Here a kinetic theory approach[61] is used in the present study. The analysis proceeds by constructing an approximate molecular velocity distribution adjacent to the liquid surface. Equations describing the conservation of mass, momentum and energy across the Knudsen layer are developed in terms of this velocity distribution. This gives Eqs. (19) and (20), as given below, for gas temperature, T_K, and density, ρ_K, outside of the Knudsen layer as functions of the liquid surface temperature and the corresponding saturation density, ρ_{sat}.

$$\frac{T_K}{T_L}=\left[\sqrt{1+\pi\left(\frac{\gamma-1}{\gamma+1}\frac{m}{2}\right)^2}-\sqrt{\pi}\frac{\gamma-1}{\gamma+1}\frac{m}{2}\right]^2 \tag{19}$$

$$\frac{\rho_K}{\rho_{sat}}=\sqrt{\frac{T_L}{T_K}}\left[\left(m^2+\frac{1}{2}\right)e^{m^2}erfc(m)-\frac{m}{\sqrt{\pi}}\right]+\frac{1}{2}\frac{T_L}{T_K}\left[1-\sqrt{\pi}me^{m^2}erfc(m)\right] \tag{20}$$

The quantity, *m*, is closely related to the Mach number at the outer edge of the Knudsen layer, M_K, and is defined as, $m=u_K/\sqrt{2R_VT_K}=M_K\sqrt{2/\gamma_V}$, where γ_V and R_V are the ratio of specific heats and the gas constant for the vapor, respectively. The value of m depends on the gas dynamics of the vapor flow away from the surface. The gas temperature, pressure and density throughout the vapor region (outside of the Knudsen layer) are uniform. The contact discontinuity, that is, the boundary between vapor and air, is an idealization that results due to the neglect of mass diffusion and heat conduction. The velocity and pressure are equal in these regions, $u_K=u_S$ and $P_K=P_S$, where the subscript, *S*, denotes properties behind the shock wave. Note that, in general, $T_K\neq T_S$ and $\rho_K\neq\rho_S$.

The thermodynamic state and velocity of the air on each side of the shock wave are related by the Rankine-Hugoniot relations, where the most convenient forms to this application are given by Eqs. (21) and (22). M_K is the Mach number in the vapor, $M_K=u_K/\sqrt{2\gamma_VR_VT_K}$.

$$\frac{P_S}{P_\infty}=1+\gamma M_K\sqrt{\frac{\gamma_VR_VT_K}{\gamma_\infty R_\infty T_\infty}}\left[\frac{\gamma_\infty+1}{4}M_K\sqrt{\frac{\gamma_VR_VT_K}{\gamma_\infty R_\infty T_\infty}}+\sqrt{1+\left(\frac{\gamma_\infty+1}{4}M_K\sqrt{\frac{\gamma_VR_VT_K}{\gamma_\infty R_\infty T_\infty}}\right)^2}\right] \tag{21}$$

$$\frac{T_S}{T_\infty}=\frac{P_S}{P_\infty}\left(1+\frac{\gamma+1}{\gamma-1}\frac{P_S}{P_\infty}\right)/\left(\frac{\gamma+1}{\gamma-1}+\frac{P_S}{P_\infty}\right) \tag{22}$$

The saturation pressure, P_{sat}, is obtained from Eq. (23), where *A*, *B* and *C* are constants which depend on the material. This is used to obtain the saturation density, $\rho_{sat}=P_{sat}/\left(R_VT_L\right)$, assuming an ideal gas.

$$\log\left(P_{sat}\right)=-\frac{A}{T_L}-B\log\left(T_L\right)+C \tag{23}$$

Eqs. (20)-(23) are solved as a function of T_L using an iterative solution method. The vapor was assumed to be iron in the form of a monatomic gas with a molecular weight of 56, and $\gamma_V=1.67$. Quantities of particular interest are the recoil pressure, P_r, and rate of energy loss due to evaporation, q_e, and they are given below.

$$P_r = P_K + \rho_K u_K^2, \qquad q_e = H_V \rho_K u_K \tag{24}$$

2.6. Laser-plasma interaction and multiple reflections of laser beam in keyhole

In the keyhole, the laser beam is reflected and absorbed multiple times on the keyhole wall. Each time when the laser beam travels inside the keyhole, it will interact with the keyhole plasma. Multiple reflections of the laser beam and its absorption mechanism are critical in determining the energy transfer in laser welding, which are discussed below.

Inverse Bremsstrahlung (IB) absorption

With the continuous heating of the laser beam, the temperature of the metal vapor inside the keyhole can reach much higher than the metal evaporation temperature, resulting in strong ionization, which produces keyhole plasma. The resulting plasma absorbs laser power by the effect of Inverse Bremsstrahlung (IB) absorption. Eqs. (25) and (26) define the IB absorption fraction of laser beam energy in plasma by considering multiple reflection effects[62]:

$$\alpha_{iB,1} = 1 - \exp\left(-\int_0^{s_0} k_{pl} ds \right) \tag{25}$$

$$\alpha_{iB,mr} = 1 - \exp\left(-\int_0^{s_m} k_{pl} ds \right) \tag{26}$$

here, $\alpha_{iB,1}$ is the absorption fraction in plasma due to the original laser beam; $\alpha_{iB,mr}$ is the absorption fraction due to the reflected laser beam. $\int_0^{s_0} k_{pl} ds$ and $\int_0^{s_m} k_{pl} ds$ are, respectively, the optical thickness of the laser transportation path for the first incident and multiple reflections, and k_{pl} is the plasma absorption coefficient due to inverse Bremsstrahlung absorption[63]:

$$k_{pl} = \frac{n_e n_i Z^2 e^6 2\pi}{6\sqrt{3} m \varepsilon_0^3 ch\omega^3 m_e^2} \left(\frac{m_e}{2\pi k T_e} \right)^{0.5} \left[1 - \exp\left(-\frac{\omega}{k T_e} \right) \right] \bar{g} \tag{27}$$

where Z is the average ionic charge in the plasma, ω is the angular frequency of the laser radiation, ε_0 is the dielectric constant, k is the Boltzmann's constant, n_e and n_i are particle densities of electrons and ions, h is Planck's constant, m_e is the electron mass, T_e is the excitation temperature, c is the speed of light, and $\bar{g}$ is the quantum mechanical Gaunt factor. For the weakly ionized plasma in the keyhole, the Saha equation[63] can be used to calculate the densities of plasma species:

$$\frac{n_e n_i}{n_0} = \frac{g_e g_i}{g_0} \frac{\left(2\pi m_e k T_e\right)^{1.5}}{h^3} \exp\left(-\frac{E_i}{kT_e}\right) \tag{28}$$

Fresnel absorption

As discussed before, part of the laser energy will be absorbed by keyhole plasma and part of the laser energy can reach the keyhole wall directly. So, the energy input (q_{laser}) for the keyhole wall consists of two parts: 1) Fresnel absorption of the incident intensity directly from the laser beam ($I_{\alpha,Fr}$) and 2) Fresnel absorption due to multiple reflections of the beam inside the keyhole ($I_{\alpha,mr}$).

$$q_{laser} = I_{\alpha,Fr} + I_{\alpha,mr} \tag{29}$$

$$I_{\alpha,Fr} = I_{laser} \cdot (1-\alpha_{iB,1}) \cdot \alpha_{Fr}(\varphi_1) \tag{30}$$

$$I_{\alpha,mr} = \sum_{mr=1}^{n} I_{laser} \cdot (1-\alpha_{iB,1}) \cdot (1-\alpha_{Fr}) \cdot (1-\alpha_{iB,mr}) \cdot \alpha_{Fr}(\varphi_{mr}) \tag{31}$$

where I_{laser} is the incoming laser intensity. We assume the laser beam has in the simplest case a Gaussiam-like distribution:

$$I_{laser}(x,y,z) = I_0 \left(\frac{r_f}{r_{f0}}\right)^2 \exp\left(-\frac{2r^2}{{r_f}^2}\right) \tag{32}$$

where r_f is the beam radius and r_{f0} is the beam radius at the focal position; I_0 is the peak intensity. α_{Fr} is the Fresnel absorption coefficient and can be defined it in the following formula[64]:

$$\alpha_{Fr}(\varphi) = 1 - \frac{1}{2}\left(\frac{1+(1-\varepsilon\cos\varphi)^2}{1+(1+\varepsilon\cos\varphi)^2} + \frac{\varepsilon^2 - 2\varepsilon\cos\varphi + 2\cos^2\varphi}{\varepsilon^2 + 2\varepsilon\cos\varphi + 2\cos^2\varphi}\right) \tag{33}$$

where φ is the angle of incident light with the normal of keyhole surface, n is the total number incident light from multiple reflections, $\vec{I}$ is the unit vector along the laser beam radiation direction and $\vec{n}$ is unit vector normal to the free surface. ε is a material-dependent coefficient.

2.7. Radiative heat transfer in laser-induced plasma

When an intense laser beam interacts with metal vapor, a significant amount of the laser radiation is absorbed by the ionized particles. The radiation absorption and emission by the vapor plume may strongly couple with the plume hydrodynamics. This coupling, shown on the right-hand side of Eq. (7), will affect the plasma laser light absorption and radiation cooling terms. The radiation source term $\nabla \cdot (-\mathbf{q_r})$ is defined via

$$\nabla \cdot \mathbf{q_r} = k_a(4\pi I_b - \int_{4\pi} I d\Omega) \tag{34}$$

where k_a, I_b and Ω denote the Planck mean absorption coefficient, blackbody emission intensity and solid angle respectively. For the laser-induced plasma inside the keyhole, the scattering effect is not significant compared with the absorbing and emitting effect. So it will not lead to large errors to assume the plasma is an absorbing-emitting medium. The radiation transport equation (RTE) has to be solved for the total directional radiative intensity I[65]:

$$(\mathbf{s} \cdot \nabla) I(\mathbf{r}, \mathbf{s}) = k_a(I_b - I(\mathbf{r}, \mathbf{s})) \tag{35}$$

where **s** and **r** denote a unit vector along the direction of the radiation intensity and the local position vector. The Planck mean absorption coefficient is defined in the following[65]:

$$k_a = \left(\frac{128}{27}k\right)^{0.5}\left(\frac{\pi}{m_e}\right)^{1.5}\frac{Z^2 e^6 \bar{g}}{h\sigma c^3}\frac{n_e n_i}{T_v^{3.5}} \tag{36}$$

where n_i and n_e represent the particle density of ions and electrons, T_v is the temperature of the plasma, Z stands for the charge of ions, e is the proton charge and m_e is the mass of electrons.

2.8. Tracking of free surfaces

The algorithm of volume-of-fluid (VOF) is used to track the moving free surface[48]. The fluid configuration is defined by a volume of fluid function, $F(x,y,z,t)$, which is used to track the location of the free surface. This function represents the volume of fluid per unit volume and satisfies the following conservation equation:

$$\frac{dF}{dt} = \frac{\partial F}{\partial t} + (\mathbf{V} \cdot \nabla)F = 0 \tag{37}$$

When averaged over the cells of a computing mesh, the average value of F in a cell is equal to the fractional volume of the cell occupied by the fluid. A unit value of F means a cell full of fluid and a zero value indicates a cell containing no fluid. Cells with F values between zero and one are partially filled with fluid and identified as surface cells.

3. Results and discussions

Based on the aforementioned scientific principles governing the hybrid laser-arc welding process, Zhou *et al*.[40,69,70] have successfully developed mathematical models to simulate the transport phenomena like heat and mass transfer, melt flow; energy transport in keyhole plasma, etc. in both pulsed and three-dimensional moving hybrid laser-MIG welding. Detailed discussions are given in the following sections.

3.1. Two-dimensional hybrid laser-MIG welding

In this study, the base metal is assumed to be a stainless steel 304 containing 100 ppm of sulfur. The laser energy is assumed to be in the Gaussian distribution and the divergence of the laser beam is negligible because the focus length of the laser beam is less than 3mm. The laser power and beam radius at the focus are 1800 W and 0.2 mm respectively. The laser power is turned on at t = 0 s and shut down at t = 15 ms. To simulate the MIG process, droplet is assumed to be spherical and is generated in a steady manner. The diameter of filler droplet is assumed to be 0.35 mm, its initial speed is 0.5 m/s right above the weld surface, its initial temperature is 2400 K, and its generation frequency is 1000 Hz. The droplet is assumed to be fed into the keyhole from the top. Droplet generation and formation are actually related to wire size and wire feed speed. Further information can be found in Ref. [13].

Fig. 5 shows the comparison of the cross-sectional view of a hybrid laser-MIG weld and a laser weld. As shown, there is a "pore" in the laser weld, which is due to the rapid solidification in laser welding. Detailed discussion on the formation of porosity in the weld can be found in Ref. [14]. It is also noticed that there are some "undercuts" near the top edge of the laser weld which is one of the major disadvantages of laser welding. In hybrid laser-MIG welding, the reason why there is no pore found in the final weld was believed to be mainly due to the addition of filler metal in the process. The momentum and energy carried by the filler droplets greatly impact the fluid flow and heat transfer in the weld pool and the shape of the solidified weld pool as well. The overall effect depends on the droplet size, droplet generation frequency and droplet generation duration as well. With an optimal operation window, a weld with desired shape and quality can be achieved in hybrid laser-MIG welding. In addition, it is found that the additional heat input from the arc in hybrid laser welding is transferred to the weld pool mainly in the region near the top of the weld, which makes the top portion of the weld wider than that in laser welding. It is further found the undercuts frequently observed in laser welding are eliminated and the shape of the final weld can be modified by the extra filler metal coming from the MIG process. However, the penetration depth in hybrid welding is noticed to be almost the same as that in laser welding, which means the penetration depth in hybrid laser-arc welding mainly depends on the laser power used, but not the arc power.

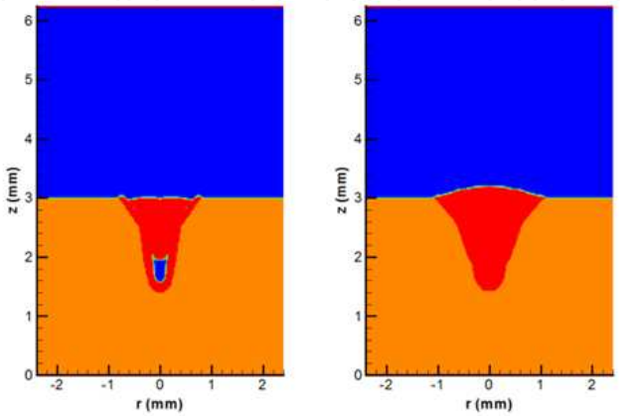

Figure 5. Comparison of weld bead shape between laser welding and hybrid laser-MIG welding.

3.2. Interaction between filler droplets and weld pool

Fig. 6 shows typical interactions between droplets and weld pool in hybrid laser-arc welding. The corresponding distributions of temperature, sulfur concentration, and melt flow velocity are given in Figs. 7, 8 and 9, respectively. Since only the interaction between filler droplets and weld pool is concerned in this discussion, the keyhole formation process is ignored which can be found in Ref. [14]. As shown in Fig. 6, after the laser is shut off at t = 15.0 ms, the laser-induced recoil pressure decreases quickly. Under the action of surface tension and hydrostatic pressure, the molten metal near the keyhole shoulder has tendency to "fill up" the keyhole. At about t = 17.5 ms, the first droplet impinges onto the liquid metal at the bottom of the keyhole. The downward momentum carried by the droplet causes the droplet liquid to flow downward and outward along the keyhole wall, which can be seen clearly by the sulfur composition shown in Fig. 8. Under the action of hydrostatic force and surface tension, the liquid along the keyhole wall has a tendency to flow downward along the keyhole wall. So the upward flow caused by the filler droplet impingement will be weakened. So when the subsequent droplets falls into the keyhole, the liquid level in the center of the keyhole rises, as shown in Fig. 6 at t = 21.5 ms. For the first several droplets, the filler metal mainly diffuses along the longitude direction. Only the first droplet can spread out along the solid-liquid interface driven by the downward momentum. However, as more and more droplets impinge into the weld pool, a vortex is created, which helps the filler metal to diffuse outwards in the latitude direction, as shown in Fig. 8.

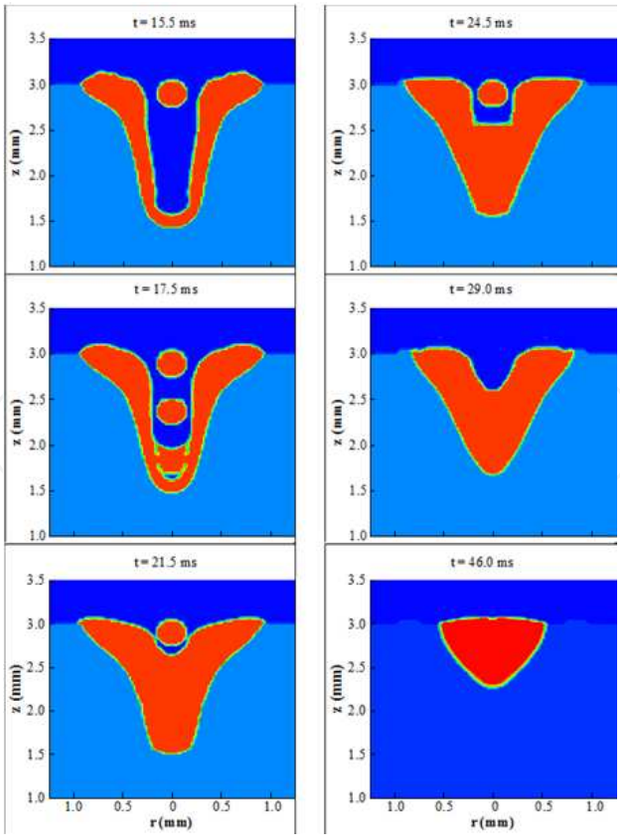

Figure 6. Droplet and weld pool interaction in hybrid laser welding.

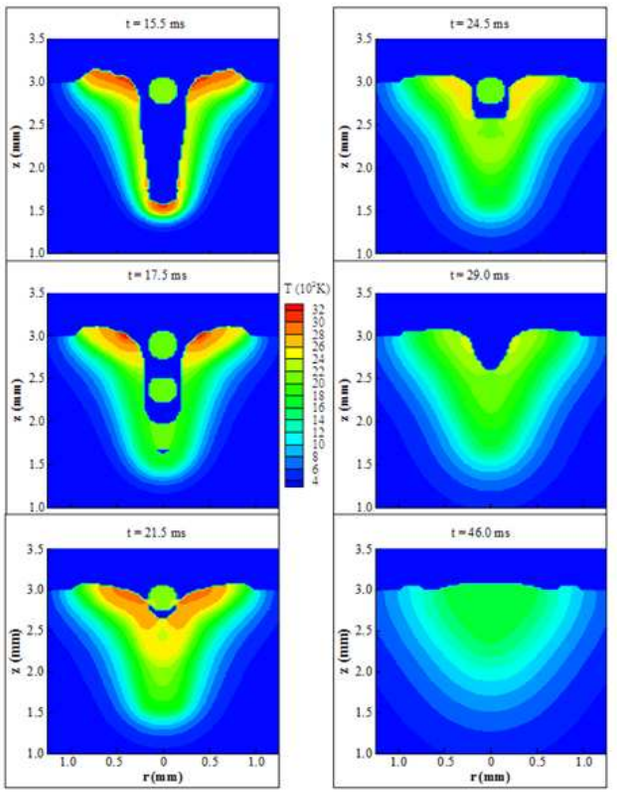

Figure 7. The corresponding temperature distributions as shown in Fig. 6.

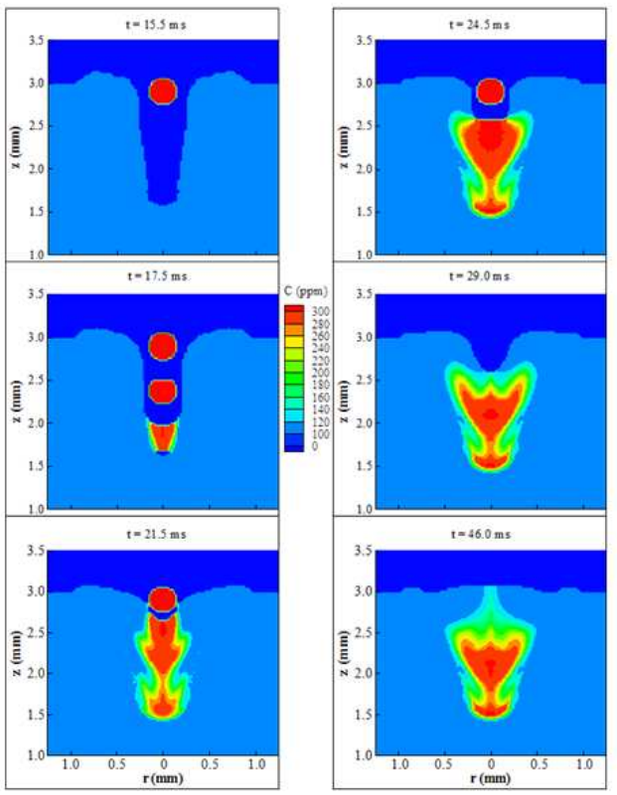

Figure 8. The corresponding sulfur concentration distributions as shown in Fig. 6

As shown in Fig. 9, there is an anticlockwise vortex in the middle waist of the keyhole. As mentioned before, the liquid on the shoulder of the keyhole has a tendency to fill back along the keyhole wall. When the droplets impinge into the keyhole, the outer liquid layer along the keyhole wall has the same flow direction as the filler metal. So the flow direction of the liquid metal here remains downward. Since the liquid is incompressible, the downward flow will push up some amount of liquid upward. The kinetic energy of the fluid flow in the center will be transferred into the potential and kinetic energy of the outward flow. So the downward momentum becomes smaller and smaller and finally it changes its direction. As shown in Fig. 9 at t = 21.5 ms, the flow direction changes from downward to outward at the bottom of the vortex and then bounds upward on the solid keyhole wall. During the upward flow process along the solid-liquid interface of the keyhole wall, the kinetic energy is transferred into the potential energy and the velocity becomes smaller and smaller. Finally the flow direction is changed to be inward by the back-filling momentum from the liquid on the shoulder of the keyhole. As droplets continue to drip into the keyhole, more and more downward momentum is added into the center of the keyhole, the vortex affected zone is enlarged and the strength of the vortex is enhanced, which helps the filler metal to distribute outward along with the vortex flow, as shown in Fig. 8. At t = 24.5 ms, the diffusion zone of filler metal is much larger compared with that at t = 21.5 ms. Since the latitude diffusion of filler metal has a close relationship with the vortex, the evolution of the vortex can be deduced from the shape of the diffusion zone of the filler metal in the final fusion zone. Moreover, at t = 24.5 ms, the downward velocity of the liquid in the center is quite large, the mass from droplets is not enough to compensate the downward mass flow in the center of the keyhole, which leaves the liquid surface decrease here.

After t = 25.0 ms, no droplet will be added into the keyhole. The fluid near the center of the keyhole is bounced back under the action of hydrostatic force and surface tension force. As shown at t = 29.0 ms in Fig. 9, the liquid in the keyhole starts to flow inward and downward, which causes the size of the keyhole to become smaller and smaller. Finally the keyhole will be filled, as shown at t = 49.0 ms in Fig. 6. During the backfill process, the vortex becomes weaker and weaker. So the diffusion of filler metal is not improved much in the latitude direction, which can be found by comparing those figures at t = 29.0 ms and at t = 46.0 ms in Fig. 5.9. Moreover, from the distribution of filler metal at t = 46.0 ms as shown in Fig. 8, it can be concluded that during the backfill process, majority of the filling metal comes from the upper shoulder of the keyhole because only a little of the filler metal is located near the center of the keyhole, which is brought here by the bouncing flow. As shown in Fig. 7, the filler droplet also brings some heat into the weld pool, which will delay the solidification process. Since the diffusion of filler in the fusion zone is greatly limited by the solidification, the delayed solidification will give more time for the filler to diffuse. After the termination of droplets, the heat input carried by droplets also decreases. Due to heat loss to the base metal through conduction and to the surroundings through radiation and convection, the size of the molten pool becomes smaller and smaller as a result of solidification. At t = 46.0 ms, the melt flow in the weld pool is almost diminished and the temperature distribution is more uniform than before, as shown in Figs. 9 and 7, respectively. The shape and composition of the weld will not change much comparing with the completely solidified one.

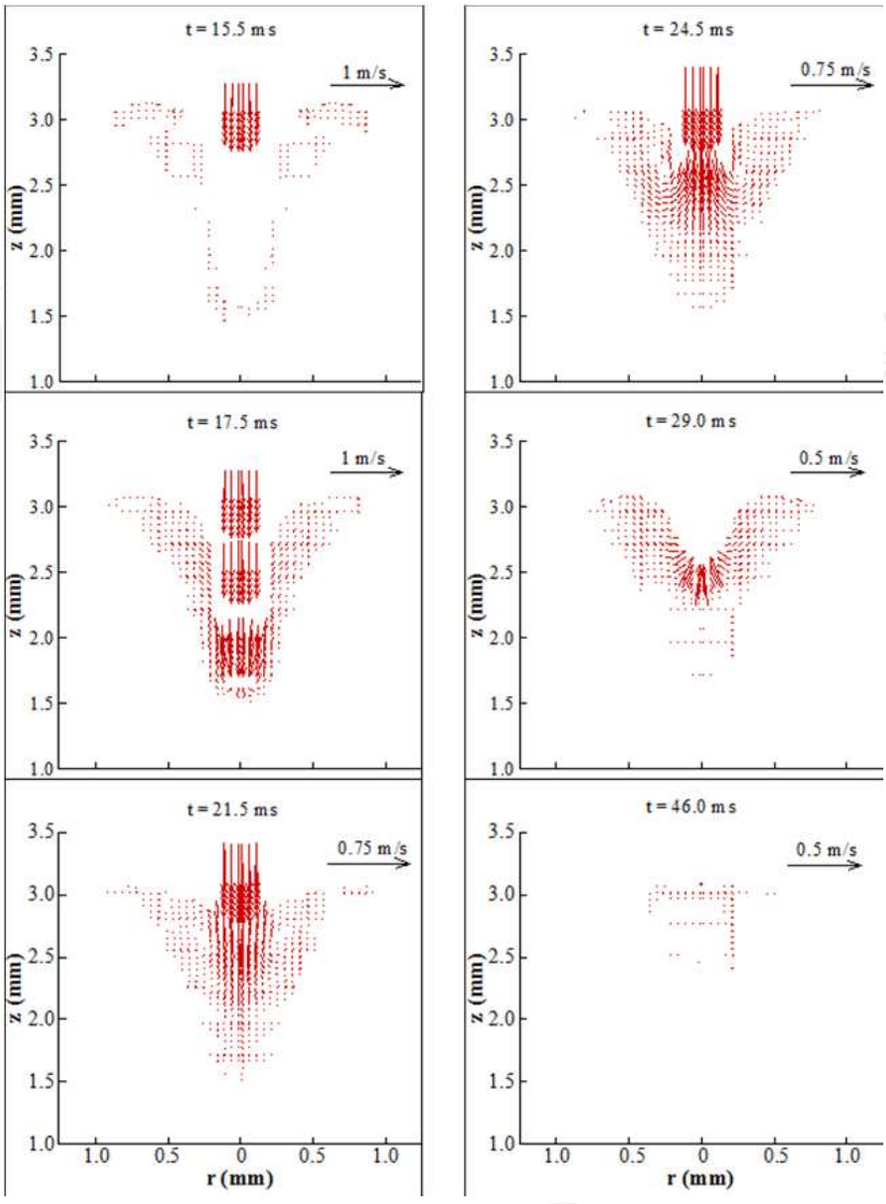

Figure 9. The corresponding velocity distributions as shown in Fig. 6.

3.3. Modification of composition by adding filler metal

Since crack sensitivity of the weld is believed to be strongly related with the composition of the weld pool, adding filler metal with anti-crack elements into the weld pool in hybrid laser welding can thus improve the weld bead quality. However, the effect depends greatly on the diffusion process in the weld pool. In the following, the effects of factors such as droplet size, droplet generation frequency, impingement velocity of the droplet and its lasting duration on the diffusion process are discussed by changing the condition of one specific parameter, while keeping the rest of the parameters unchanged. If not specially mentioned, the welding condition is defined as follows: the droplet diameter is 0.35 mm, its initial velocity is 0.5 m/s, the generation frequency is 1000 HZ and the duration of droplet feeding is 10.0 ms which starts at t = 15.0 ms and ends at t = 25.0 ms.

3.3.1. Effect of droplet size on the diffusion process in hybrid laser welding

Three studies are carried out with a droplet size of 0.3 mm, 0.35 mm and 0.4 mm respectively. As shown in Fig. 10, with the increase of droplet size, the latitude diffusion of filler metal is enlarged. From the previous discussions on the diffusion process, the latitude diffusion of the filler metal is found to be closely related to the vortex in the weld pool. The strength and the affected zone of the vortex depend on the downward momentum carried by droplets, which is the product of droplet mass and velocity. As the droplet size increases, the downward momentum increases, which will lead to a stronger vortex. So the diffusion zone is enlarged outward, especially in the middle depth of the keyhole where the vortex is located. This is clear shown by comparing those figures for d = 0.30 mm and d = 0.35 mm in Fig. 10. Meanwhile, larger downward momentum from larger droplet also leads to a strong bouncing flow near the center of keyhole after termination of droplet feeding, which helps filler metal to diffuse into the upper layer in the final weld, as shown in Fig. 10 for d = 0.40 mm. Moreover, larger droplet size brings more filler metal into the keyhole. The heat input carried by droplets also increases, which helps delay the solidification of the fusion zone. Thus, the filler metal has more time to diffuse into the weld pool before its solidification. More filler metal also helps to increase the filler concentration in the final weld. However, larger droplets also lead to some negative effects on the diffusion of filler metal near the center of the weld zone. After the termination of droplet feeding, the melt surface near the center of the keyhole will continue to go down due to the larger hydrodynamic pressure caused by the downward momentum. This will lead to a deep hole there. During the backfill process of this hole, some metal from the upper part of the keyhole may flow into the bottom part of this hole. Since the concentration of filler metal in the upper part of keyhole is very low, it leaves a low diffusion zone of filler metal in the center of the final weld, as shown in Fig. 10 for d = 0.40 mm.

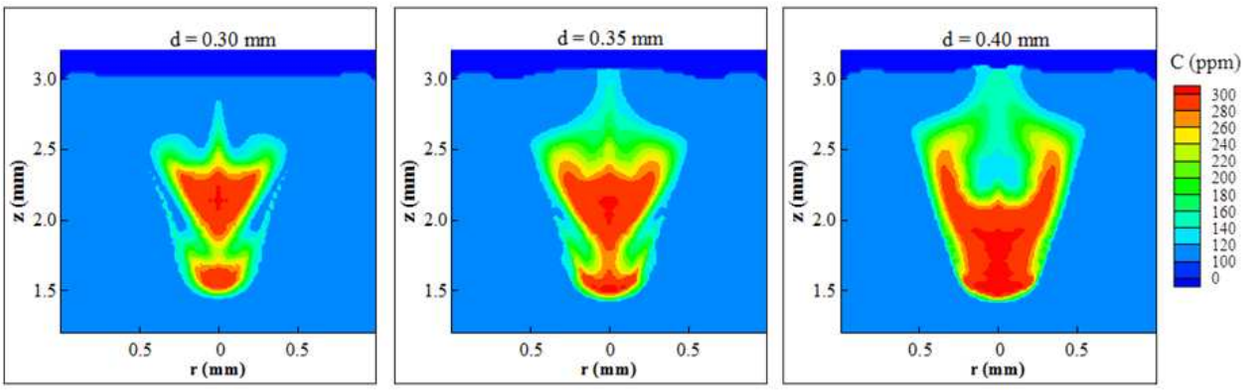

Figure 10. Effect of droplet size on diffusion process in hybrid laser welding.

3.4. Effect of droplet generation frequency on diffusion of filler metal in fusion zone

In the hybrid laser welding process, the droplet is generated at a specific frequency that is controlled by the wire feed rate. The effect of droplet generation frequency on diffusion of

filler metal in the fusion zone is shown in Fig. 11. In the study, the droplet generation frequency is 500 HZ, 667 HZ and 1000 HZ, which corresponds to the generation of one droplet every 2.0 ms, 1.5 ms and 1.0 ms. As shown, the diffusion of filler metal in the weld pool is improved with the increase of generation frequency. This can be interpreted through the above analysis on the interaction between the droplets and weld pool. As mentioned before, the latitude diffusion of filler is mainly through the vortex flow induced by the impingement of droplets. With the increase of generation frequency, more droplets fall into the weld pool per unit time, which results in higher downward momentum per unit time. So the vortex in the weld pool is enhanced, which helps the filler metal diffuse in the latitude direction. Meanwhile, the total amount of filler metal added into the weld pool also increases with higher generation frequency, which also helps increase the concentration of filler metal in the final weld and increase the diffusion time, as mentioned before. Furthermore, the longitude distribution of filler metal is found to be improved with higher generation frequency. As shown, in the case f = 500 HZ, there exists a low filler metal concentration zone in the lower part of the keyhole due to the weak strength of the vortex in the weld pool and a long delay time between the droplet generation. When frequency increases to 1000 HZ, the size of this zone is greatly reduced.

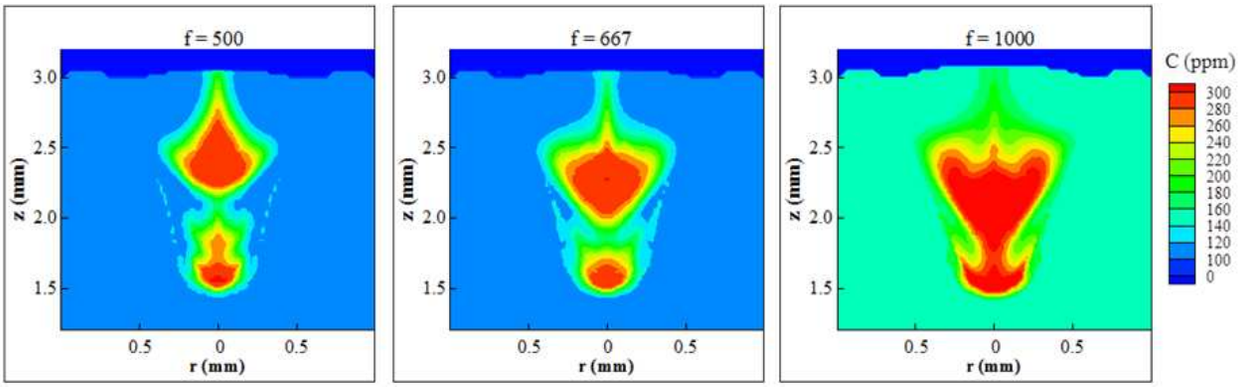

Figure 11. Effect of droplet generation frequency on diffusion process in hybrid laser welding.

3.5. Effect of droplet generation duration on diffusion of filler metal in fusion zone

In hybrid laser welding, the termination of droplet generation can be achieved through the control of removal of the filler wire. The effect of controlling the droplet generation duration on metal diffusion in the weld pool is investigated. As shown in Fig. 12, three cases are carried out with droplet generation duration at 5.0 ms, 10.0 ms and 15.0 ms, respectively. For short duration of 5.0 ms, the vortex induced by the downward momentum of the droplet is not completely developed because of lower downward momentum, which leads to poor latitude distribution of filler metal. In this case, most of the filler metal is located in the lower part of the keyhole. During the backfill process, the bounced flow is not strong enough to push the filler metal upward to the upper part of the keyhole. The keyhole is filled with the base metal liquid where no filler metal exists. So the longitude filler diffusion is also poor with a short duration of droplet generation.

With the increase of the duration length to 10.0 ms, more filler metal will fall into the keyhole. The vortex in the weld pool is enhanced with the increased downward momentum which improves the latitude diffusion. Meanwhile, the droplets are distributed along the entire depth of the keyhole, which leads to better longitude distribution of filler metal. Moreover, the total amount of filler metal also increases with the increase of duration, which also helps the diffusion of filler metal in the fusion zone, as mentioned before. So both the longitude and latitude diffusion of filler metal are improved, as shown. However, with a further longer droplet generation to 15.0 ms, the downward momentum is accumulated due to the continuous impingement of the droplets into the weld pool, which leads to a deep hole in the weld pool. During the backfill process of this hole, the filler metal is mainly located in the bottom, which cannot bounce back in time before the base metal fluid from the upper shoulder arrives at the bottom of this hole, which leaves a low diffusion zone of filler metal in the center of final weld, as shown in Fig. 12.

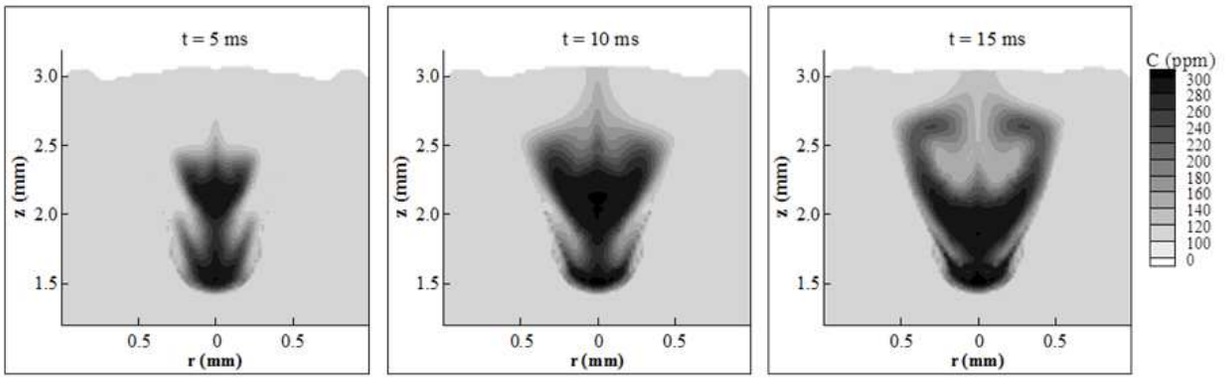

Figure 12. Effect of droplet impingement duration on diffusion process in hybrid laser welding.

3.6. Three-dimensional hybrid laser-MIG welding

Fig. 13 shows a schematic sketch of a three-dimensional hybrid laser-MIG welding. In this study, the laser power is 2.0 kW and the laser beam radius is 0.2 mm and the focal plane is on the top surface of the base metal. The laser beam is started at x = 3.75 mm. The laser beam begins to move after being held for 20.0 ms for the keyhole to reach a certain depth. The welding speed is 2.5 cm/s and the arc power is 1 kW. Droplet begins to fall onto the base metal at t = 20.0 ms and the radius of the droplet is 0.25 mm. The droplet feeding frequency is 86 Hz and its initial speed is 30 cm/s. The distance between arc center and laser beam center is 1 mm. Fig. 14 is the side-view (at Y = 0) of the hybrid laser welding process showing a sequence of a droplet impinging onto the weld pool at different times. Fig. 15 shows the corresponding sulfur concentration distribution during the hybrid welding process, indicating the mixing process in the welding. Fig. 16 shows the corresponding velocity distributions in the weld pool. As shown in Fig. 15, the filler droplet did not mix well with the base metal in this case. Most of the droplet is just stacking on the top of the weld coupon and only small amount of the filler metal is diffused into the base metal near the solid-liquid interface. The poor mixing may have been caused by the relative long distance between the laser beam and MIG arc

center. The filler droplet is impinging into the weld pool where only a small amount of liquid metal exists. Since the temperature of this part of liquid metal is low, due to the quick solidification process there, the liquid metal there solidifies very quickly. The droplet flowing downward does not have enough time to flow around and exchange the momentum and mix with the base metal before it solidifies, as shown in Fig. 16. Therefore, most of the filler metals are just stacking on top surface of the base metal.

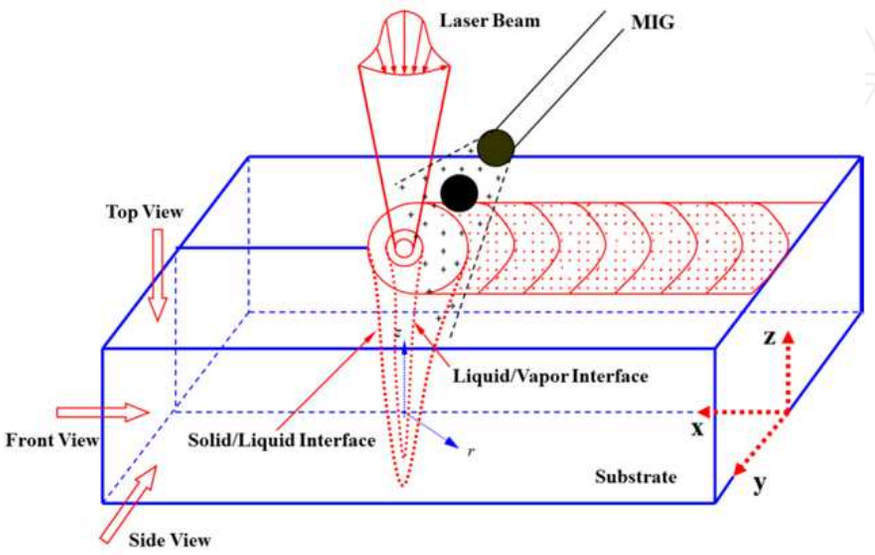

Figure 13. Schematic sketch of 3-D hybrid laser keyhole welding.

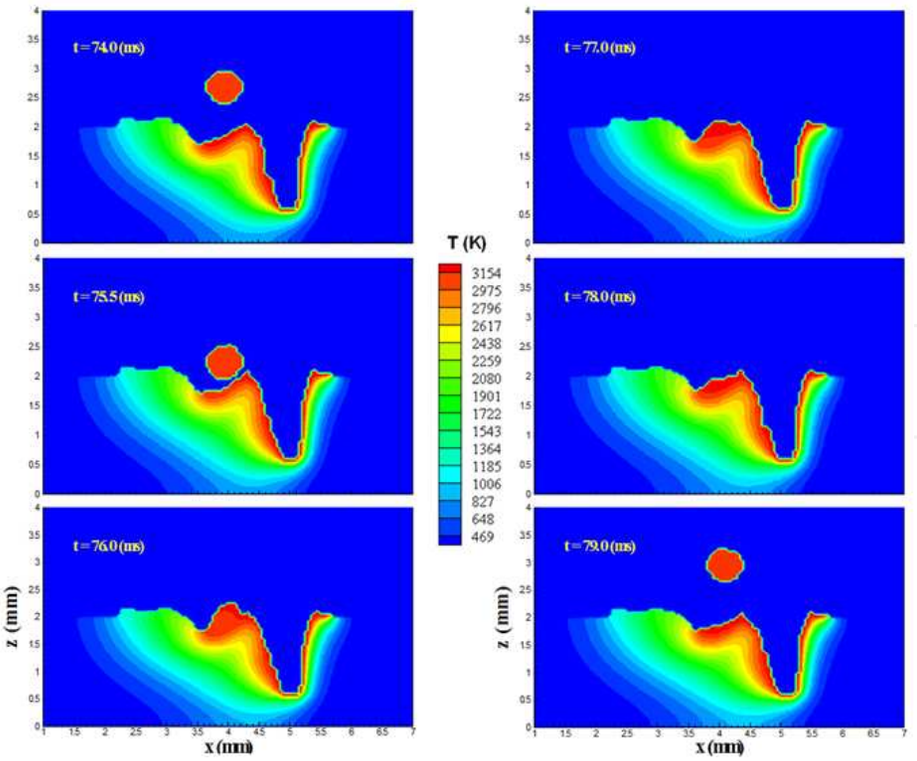

Figure 14. A typical sequence showing the impinging process and temperature distributions in 3-D moving hybrid laser keyhole welding.

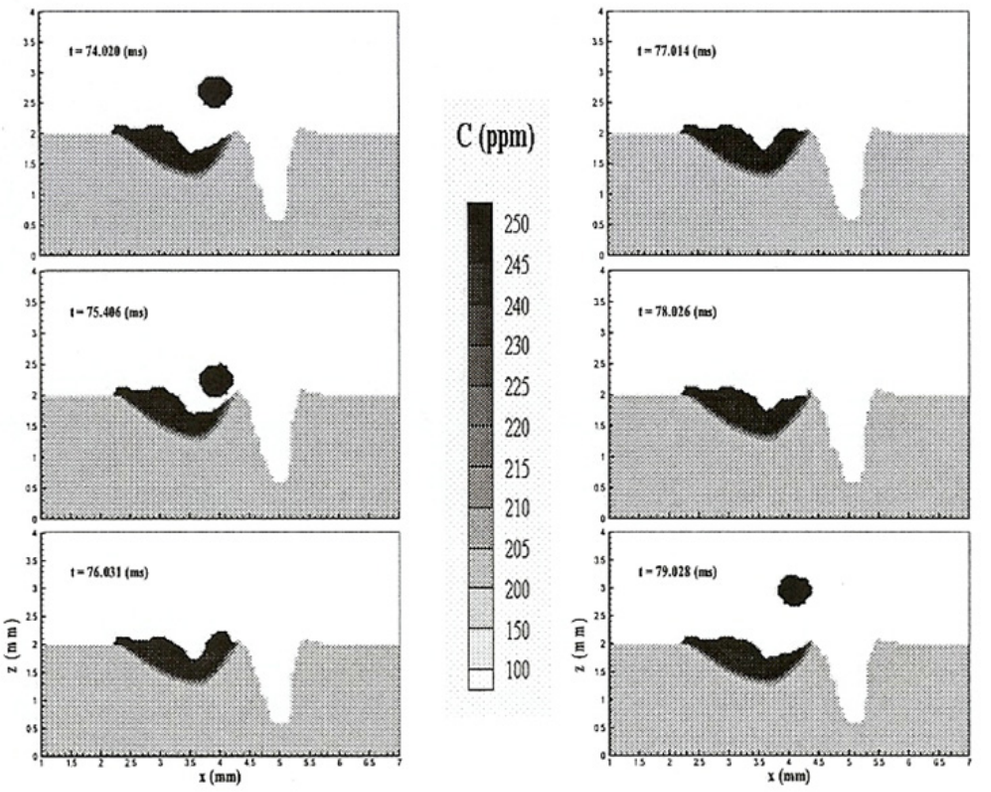

Figure 15. The corresponding sulfur concentration distributions as shown in Fig. 14.

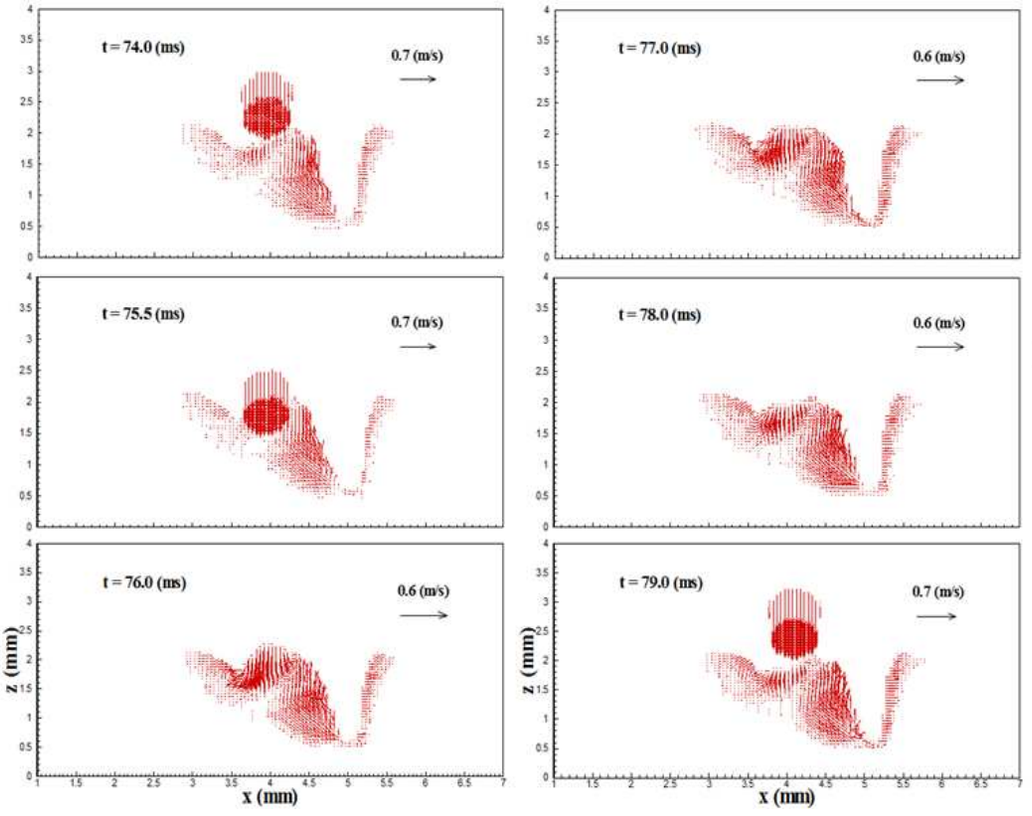

Figure 16. The corresponding velocity distributions as shown in Fig. 14.

There are a lot of process parameters which can affect the mixing of filler droplets into the weld pool in three-dimensional hybrid laser-arc welding. These include laser-arc distance, laser and arc powers, welding speed, wire feed speed and filler droplet size, etc. In the following study, the effect of laser-arc distance on diffusion is conducted by decreasing the laser-arc distance to 0.6 mm. Fig. 17 shows the mixing process during the welding. As shown, the droplet is now mixing with the base metal much better than in the previous case. In this case, since the laser-arc distance is decreased, the filler droplet can impinge into a region in the weld pool where there exists a lot of liquid metal with strong velocity and high temperature. This strong velocity liquid metal flow will interact with the impinging droplets, creating a strong momentum exchange between the droplets and weld pool, which can force the droplet to flow in all directions. Hence, a better mixing can be achieved. Also, in this case, there are more hot liquid metals in the droplet-weld pool interaction zone, thus creating relatively longer time for the droplet to mix and diffuse into the base metal. Hence, a better mixing of droplets into the weld pool is achieved.

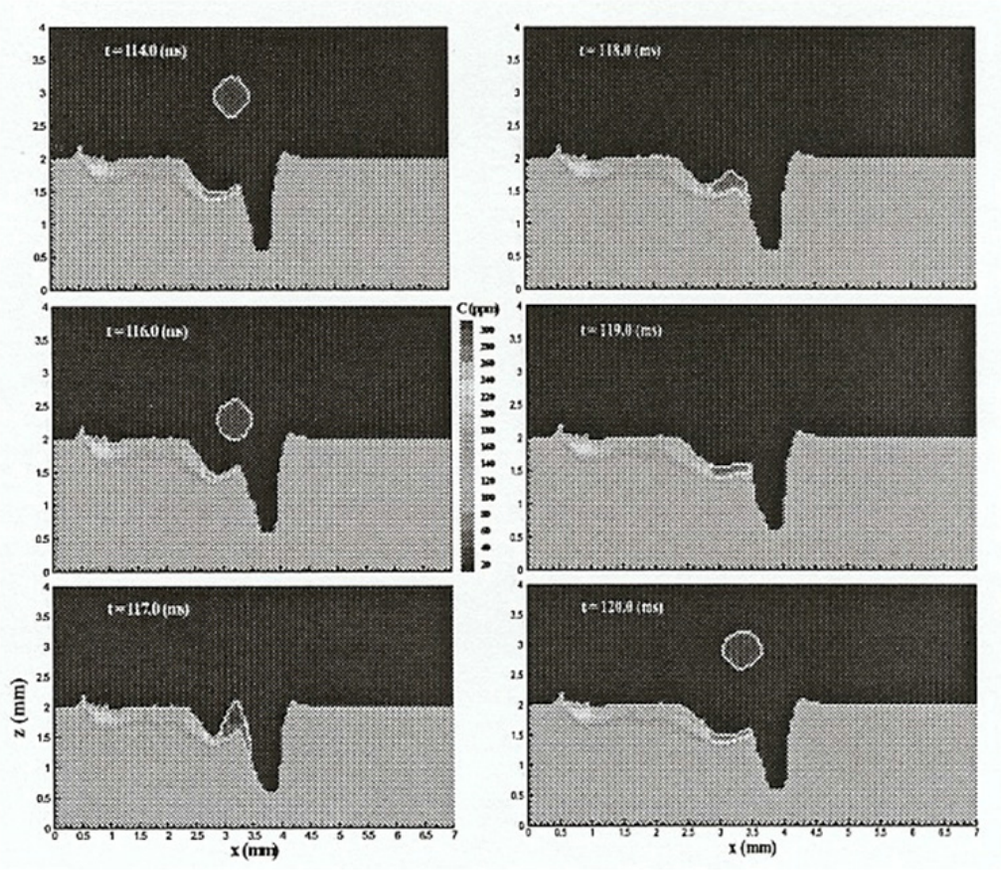

Figure 17. Diffusion process in 3-D hybrid laser keyhole welding with shorter laser-arc distance.

4. Future trends

Although hybrid laser-arc welding has been under investigation and development and gaining increasing acceptance in recent years, good understanding of the underlying physics remains a challenge. For example, the interaction between the laser and the arc has

been observed to enhance arc stability and push the arc towards the laser keyhole, resulting in a deeper penetration. However, the origin of this synergistic interaction between the arc and laser plasma is not well understood. Measuring the distributions of electron temperatures and densities in the plasma can provide a better understanding of the laser-arc interaction[9]. Porosity formation is believed to be strongly related to the keyhole collapse process. Hence, better understanding of keyhole stability and dynamics through experimental and theoretical studies would be beneficial. Hybrid welding is known to produce welds with desirable widths and depths, but the maximum gap tolerance and weld penetration for various welding conditions have not been quantified. In the future, advanced mathematical modeling of the heat transfer and fluid flow will enable accurate predictions of weld profile and cooling rates in the welding process, which is critical in understanding the evolution of weld microstructures and residual stress formation in welds. Thus, the hybrid welding process can be optimized to obtain quality welds with no cracking, no brittle phase and less thermal distortion. Better sensing and process control of the hybrid welding process would also be helpful in expanding its applications[67].

Author details

J. Zhou
Department of Mechanical Engineering, Pennsylvania State University, The Behrend College, USA

H.L. Tsai
Department of Mechanical and Aerospace Engineering,
Missouri University of Science and Technology, USA

5. References

[1] Tusek, J., and Suban, M., 'Hybrid welding with arc and laser beam', *Science and Technology of Welding and Joining*, 4(5), 308-311, 1999.
[2] Mahrle, A., and Beyer, E., 'Hybrid laser beam welding – Classification, characteristics, and applications', *Journal of Laser Applications*, 18(3), 169-180, 2006.
[3] Steen, W.M., 'Arc-augmented laser processing of materials' *J. Appl. Phys.*, 51, 5636–5641, 1980.
[4] Campana, G., Fortunato, A., Ascari, A., Tani, G., and Tomesani, L., 'The influence of arc transfer mode in hybrid laser-MIG welding,' *J. Mater. Process. Technol.*, 191, 111–113, 2007.
[5] Casalino, G., 'Statistical analysis of MIG-laser CO2 hybrid welding of Al–Mg alloy', *J. Mater. Process. Technol.*, 191, 106–110, 2007.
[6] Hu, B., and Richardson, I.M., 'Microstructure and mechanical properties of AA7075(T6) hybrid laser/GMA welds', *Material Science Engineering A*, 459, 94-100, 2007.
[7] Feng, Z.L., *Processes and mechanisms of welding residual stress and distortion*, Woodhead Publishing Ltd, Cambridge, England, 2005.
[8] Metzbower, E.A., Denney, P.E., Moon, D.W., Feng, C.R., and Lambrakos, S.G., 'Thermal analysis and microharness maping in hybrid laser welds in a structural steel', *Materials Science Forum*, 426-432, 4147-4152, 2003.

[9] Ribic, B., Palmer, T.A., and Debroy, T., 'Problems and issues in laser-arc hybrid welding', *International Materials Reviews*, 54(4), 223-244, 2009.
[10] G. Song, L. M. Liu and P. C. Wang: *Material Science Engineering A*, 429, 312–319, 2006.
[11] Nonn, A., Dahl, W., and Bleck, W., 'Numerical modelling of damage behaviour of laser-hybrid welds', *Engineering Fracture Mechanics*, 75, 3251–3263, 2008.
[12] Pinto, H., Pyzalla, A., Hackl, H., and Bruckner, J., 'A Comparative Study of Microstructure and Residual Stresses of CMT-, MIG- and Laser-Hybrid Welds', *Materials Science Forum*, 524–525, 627–632, 2006.
[13] Zhang, J. X., Xue, Y., and Gong, S. L., 'Residual welding stresses in laser beam and tungsten inert gas weldments of titanium alloy', *Science and Technology of Welding & Joining*, 10, 643–646, 2005.
[14] Liu, L.M., Song, G., and Wang, J.F.,'', *Materials Science Forum*, 488–489, 361–364, 2005.
[15] Liu, L.M., Song, G., Liang, G.L., and Wang, J.F, 'Pore formation during hybrid laser tungsten inert gas arc welding of magnesium alloy AZ31B – mechanism and remedy', Material *Science and Engineering A*, 390, 76-80, 2005.
[16] Katayama, S., Uchiumi, S., Mizutani, M., Wang, J., and Fujii, K., 'Penetration and porosity prevention mechanism in YAG laser-MIG hybrid welding', *Welding International*, 21, 25–31, 2007.
[17] Fellman, A., and Kujanpaa, V., 'The effect of shielding gas composition on welding performance and weld properties in hybrid CO2 laser-gas metal arc welding of carbon manganese steel', *Journal of Laser Applications*, 18, 12–20, 2006.
[18] Kim, T., Suga, Y., and Koike, T., 'Welding of thin steel plates by hybrid welding process combined TIG arc with YAG laser', *JSME International Journal Series A*, 46A, 202–207, 2003.
[19] Kim, Y. P., Alam, N., and Bang, H. S., 'Observation of hybrid (cw Nd:YAG laser + MIG) welding phenomenon in AA5083 butt joints with different gap conditions', *Science and Technology of Welding & Joining*, 11(3), 295–307, 2006.
[20] Murakami, K., Mitooka, Y., Hino, M., Iogawa, H., Ono, H., and Katayama, S., '', *J. Japn. Inst. Met.*, 70, 134–137, 2006.
[21] Qin, G. L., Lei, Z., and Lin, S. Y., 'Effects of Nd:YAG laser + pulsed MAG arc hybrid welding parameters on its weld shape', *Science and Technology of Welding & Joining*, 12(2), 79–86, 2007.
[22] Swanson, P. T., Page, C. J., Read, E., and Wu, H. Z., 'Plasma augmented laser welding of 6 mm steel plate ', *Science and Technology of Welding & Joining*, 12(2), 153–160, 2007.
[23] Eboo, M., Steen, W.M., and Clarke, J., 'Arc-augmented laser welding', *Advances in Welding Processes*, Proc. of the 4th Int. Conf., Harrogate, UK, 257–265, 1978.
[24] Steen, W. M., and Eboo, M., 'Arc augmented laser welding', *Metal Construction*, 11, 332–335, 1979.
[25] Bagger, C., and Olson, F.O., 'Review of laser hybrid welding', *Journal of Laser Applications*, 17(1), 2-14, 2005.
[26] Cui, H., Decker, I., and Ruge, J., 'Wechselwirkungen zwischen WIGSchweißlichtbogen und fokussiertem Laserstrahl', *Proc. of the Conference Laser'89* , Springer, Berlin, 577–581, 1989.

[27] Finke, B. R., Stern, F., and Decker, I., 'Auswirkungen eines unterstützenden Laserstrahls auf den WIG-Schweißprozess," *DVS-Ber.*, 135, 149–152, 1991.
[28] Cui, H., Decker, I., Pursch, H., Ruge, J., Wendelstorf, J., and Wohlfahrt, H., 'Laserinduziertes Fokussieren des WIG-Lichtbogens', *DVS-Ber.*, 146, 139–143, 1992.
[29] Dilthey, U., Lüder, F., and Wieschemann, A., 'Expanded capabilities in the welding of aluminium alloys with the laser-MIG hybrid process', *Aluminium*, 75, 64–75, 1999.
[30] Graf, T., and Staufer, H., 'Laser hybrid process at Volkswagen', *International Institute of Welding*, IIW-Doc. XII-1730-02, 1999.
[31] Jokinen, T., Vihervä, T., Riikonen, H., and Kujanpä, V., 'Welding of ship structural steel A36 using a Nd:YAG laser and gas metal arc welding', *Journal of Laser Applications*, 12, 185–188, 2000.
[32] Höfemann, M., Fersini, M., Szinyur, J., Haferkamp, H., and Cordini, P., 'Laser-GMA-hybrid welding of zinc-coated steel for hydroforming applications', *Proc. of the 1st Int. WLT-Conf. on Lasers in Manufacturing*, Munich, Germany, 466–472, 2001.
[33] Dilthey, U., and Keller, H., 'Prospects in laser GMA hybrid welding of steel', *Proc. of the 1st Int. WLT-Conf. on Lasers in Manufacturing*, Munich, Germany, 453–465, 2001.
[34] Waltz, C., Seefeld, T., and Sepold, G., 'Laser-GMA welding and its influence on bead geometry and process stability', *Proc. of the 1st Int. WLT-Conf. on Lasers in Manufacturing*, Munich, Germany, 444–452, 2001.
[35] Shibata, K., Sakamoto, H., and Iwase, T., 'Laser-MIG hybrid welding of aluminium alloys', *Proc. of the 1st Int. WLT-Conf. on Lasers in Manufacturing*, Munich, Germany, 436–443, 2001.
[36] Jokinen, T., Jernström, P., Karhu, M., Vanttaja, I., and Kujanpää, V., 'Optimisation of parameters in hybrid welding of aluminium alloy', *Proc. Of the 1st Int. Symp. on High Power Laser Macroprocessing*, Proc. SPIE 4831, 307–312, 2003.
[37] Ishide, T., Tsubota, S., and Watanabe, M., 'Latest MIG, TIG Arc-YAG laser hybrid welding systems for various welding products', *Proc. of the 1st Int. Symp. on High Power Laser Macroprocessing*, 2003 Proc. SPIE 4831, 347–352,2003.
[38] Hyatt, C. V., Magee, K. H., Porter, J. F., Merchant, V. E., and Matthews, J. R., 'Laser-assisted gas metal arc welding of 25-mm-thick HY-80 plate', *Welding Journal Symposium*, Miami, FL, U. S.A, 163s–172s, 2001.
[39] Fellman, A., Jernstrøm, P., and Kujanpää, V., 'The effect of shielding gas composition in hybrid welding of carbon steel', *Proceedings 9th NOLAMP, Conference on Laser Materials Processing in the Nordic Countries*, Trondheim, Norway, 103–112, 2003.
[40] Zhou, J., and Tsai, H.L., 'Modeling of transport phenomena in hybrid laser-MIG keyhole welding', *International Journal of Heat and Mass Transfer*, 51, 4353-4366, 2008.
[41] Page, C. J., Devermann, T., Biffin, J., and Blundell, N., 'Plasma augmented laser welding and its applications ', *Science and Technology of Welding & Joining*, 7(1), 1–10, 2002.
[42] S. M. Joo, Y. P. Kim, C. S. Ro, H. S. Bang and J. U. Park, '', *Adv. Nondestr. Eval.*, 270–273, 2383–2388, 2004.
[43] Graf, T., and Staufer, H., 'Laser-hybrid welding drives VW improvements', *Welding Journal*, 82, 42–48, 2003.

[44] Ono, M., Shinbo, Y., Yoshitake, A., and Ohmura, M., 'Welding properties of thin steel sheets by laser-arc hybrid welding: laser-focused arc welding', *Proc. 1st Int. Symp. on 'High-power laser macroprocessing'*, Osaka, Japan, 369–374, 2002.
[45] Song, G., Liu, L. M., Chi, M. S., and Wang, J. F., 'Investigations of Laser-TIG Hybrid Welding of Magnesium Alloys', *Materials Science Forum*, 488–489, 371–375, 2005.
[46] Chiang, K.C., Tsai, H.L., 'Shrinkage-induced fluid flow and domain change in two-dimensional alloy solidification', *Int. J. Heat and Mass Transfer*, 35, 1763-1769, 1992.
[47] Zhou, J., Tsai, H.L., and Wang, P.C., 'Transport Phenomena and Keyhole Dynamics during Pulsed Laser Welding', *ASME Journal of Heat Transfer*, 128(7), 680-690, 2006.
[48] Wang, Y., 'Modeling of three-dimensional gas metal arc welding process', *Ph.D. Thesis*, University of Missouri-Rolla, 1999.
[49] Lowke, J.J., Kovitya, P., and Schmidt, H.P., 'Theory of free-burning arc columns including the influence of the cathode', *J. Phys. D: Appl. Phys.*, 25, 1600-1606, 1992.
[50] Haidar, J., 'A theoretical model for gas metal arc welding and gas tungsten arc welding', *J. Appl. Phys.*, 84, 3518-3529, 1998.
[51] Haidar, J., Lowke, J.J., 'Predictions of metal droplet formation in arc welding', *J. Appl. Phys. D: Appl. Phys.*, 29, 2951-2960, 1996.
[52] Haidar, J., 'An analysis of the formation of metal droplets in arc welding', *J. Phys. D: Appl. Phys.*, 1233-1244, 1998.
[53] Haidar, J., 'Prediction of metal droplet formation in gas metal arc welding. II.', *J. Appl. Phys.*, 84, 3530-3540, 1998.
[54] Haidar, J., 'An analysis of heat transfer and fume production in gas metal arc welding. III.', *J. Appl. Phys.*, 85, 3448-3459, 1998.
[55] Lowke, J.J., Kovitya, P., and Schmidt, H.P., 'Theory of free-burning arc columns including the influence of the cathode', *J. Phys. D: Appl. Phys.*, 25, 1600-1606, 1995.
[56] Zhu, P., Lowke, J.J., Morrow, R., 'A unified theory of free burning arcs, cathode sheaths and cathodes', *J. Phys. D: Appl. Phys.*, 25, 1221-1230, 1992.
[57] Brackbill, J.U., Kothe, D.B., and Zemach, C., 'A continuum method for modeling surface tension', *J. of Computational Physics*, 100, 335-354, 1992.
[58] Fan, H.G., and Kovacevic, R., 'Droplet formation, detachment, and impingement on the molten pool in gas metal arc welding', *Metall. Trans.*, 30B, 791–801, 1999.
[59] Anisimov, S.I., 'Vaporization of metal absorbing laser radiation', *Soviet Physics*, JETP 27 (1), 182-183, 1968.
[60] Knight, C.J., 'Theoretical modeling of rapid surface vaporization with back pressure', *AIAA J.*, 17(5) 519-523, 1979.
[61] Kanouff, M.P., Kassinos, A., Noble, D.R., and Schunk, P.R., 'Laser spot weld modeling using an ALE finite element method', Sandia National Laboratories Report.
[62] Kaplan, A., 'A model of deep penetration laser welding based in calculation of the keyhole profile', *J. Phys. D: Appl. Phys.*, 27, 1805-1814, 1994.
[63] Duley, W., *Laser welding*, John Wiley & Sons, 1999.
[64] Ducharme, R., Williams, K., Kapadia, P., Dowden, J., Steen, B., and Glowacki, M., 'The laser welding of thin metal sheets: an integrated keyhole and weld pool model with supporting experiments', *J. Phys. D: Appl. Phys.*, 27, 1619-1627, 1994.

[65] Ho, J.R., Grigoropoulos, C.P., Humphrey, J.A.C., 'Gas dynamics and radiation heat transfer in the vapor plume produced by pulsed laser irradiation of aluminum', *J. Appl. Phys.*, 79, 7205-7215, 1996.
[66] Bagger, C., Olsen, F.O., 'Review of hybrid laser welding', *J. Laser Appl.*, 17, 2-14, 2005.
[67] Ribic, B., Palmer, T.A., DebRoy, T., 'Problems and issues in laser-arc hybrid welding', *Int. Mater. Rev.*, 54 (4), 223-244, 2009.
[68] Kong, F. and Kovacevic, R., '3D Finite Element Modeling of the Thermally Induced Residual Stress in the Hybrid Laser/Arc Welding of Lap Joint', *Journal of Materials Processing Technology*, 941-950, 2010.
[69] Zhou, J., Zhang, W. H., Tsai, H. L., Marin, S. P., Wang, P. C., and Menassa, R., 'Modeling the transport phenomena during hybrid laser-MIG welding process', *Proceedings IMECE'03, ASME International Mechanical Engineering Congress & Exposition*, Washington, DC, IMECE2003-41763, 1-8, 2003.
[70] Zhou, J., and Tsai, H. L., 'Investigation of mixing and diffusion processes in hybrid spot laser – MIG keyhole welding', *Journal of Physics D: Applied Physics*, 42, 1-15, 2009.

IntechOpen